



# Benchmarking the performance of all-solid-state lithium batteries

Simon Randau<sup>1</sup>, Dominik A. Weber<sup>1,4</sup>, Olaf Kötz<sup>1</sup>, Raimund Koerver<sup>1,5</sup>, Philipp Braun<sup>2</sup>, André Weber<sup>1,2</sup>, Ellen Ivers-Tiffée<sup>2</sup>, Torben Adermann<sup>3</sup>, Jörn Kulisch<sup>3</sup>, Wolfgang G. Zeier<sup>1</sup>, Felix H. Richter<sup>1</sup>✉ and Jürgen Janek<sup>1</sup>✉

**Increasing the specific energy, energy density, specific power, energy efficiency and energy retention of electrochemical storage devices are major incentives for the development of all-solid-state batteries. However, a general evaluation of all-solid-state battery performance is often difficult to derive from published reports, mostly due to the interdependence of performance measures, but also due to the lack of a basic reference system. Here, we present all-solid-state batteries reduced to the bare minimum of compounds, containing only a lithium metal anode,  $\beta$ -Li<sub>3</sub>PS<sub>4</sub> solid electrolyte and Li(Ni<sub>0.6</sub>Co<sub>0.2</sub>Mn<sub>0.2</sub>)O<sub>2</sub> cathode active material. We use this minimalistic system to benchmark the performance of all-solid-state batteries. In a Ragone-type graph, we compare literature data for thiophosphate-, oxide-, phosphate- and polymer-based all-solid-state batteries with our minimalistic cell. Using fundamental equations for key performance parameters, we identify research targets towards high energy, high power and practical all-solid-state batteries.**

Electrochemical energy storage devices, such as rechargeable batteries, are increasingly important for mobile applications as well as for grid-scale stationary storage. Batteries with simultaneously high energy, power, energy efficiency and energy retention are generally preferred. Lithium-ion battery technology, which uses organic liquid electrolytes, is currently the best-performing energy storage method, especially for powering mobile applications and electric vehicles<sup>1</sup>.

However, the recent discovery of new types of highly lithium-ion conducting solid electrolytes has triggered a surge of interest in the all-solid-state battery (ASSB)<sup>2</sup>. In particular, thiophosphate-based solid electrolytes with high ionic conductivity have been developed to reduce internal resistance and improve the rate performance of ASSBs<sup>3</sup>. Oxide-, phosphate- and polymer-based electrolytes have also been developed to create ASSBs, with graphite or lithium metal anode active material (AAM) and intercalation- or conversion-type cathode active material (CAM)<sup>4–7</sup>. Improvements in rate performance<sup>3</sup> due to the large lithium transfer number of most solid electrolytes and potentially negligible interface resistance with AAMs, such as graphite<sup>3</sup> or lithium<sup>8</sup>, may result in ASSB cell performance exceeding that of lithium-ion batteries<sup>9</sup>.

A central goal in the development of next-generation battery technologies is to maximize the attainable specific energy (cell energy per cell mass) and energy density (cell energy per cell volume). One path to increasing these is by maximizing the anode capacity by using solely lithium metal as the AAM<sup>10</sup>. However, the implementation of a lithium metal anode is hampered by interface reactions, which degrade cell performance, and by dendrite-like growth of lithium, which short-circuits the cells during battery operation<sup>11,12</sup>. Therefore, protective coatings that modify the anode and cathode interfaces with the solid electrolyte are developed to achieve ASSBs with minimized internal resistance and stable cycling<sup>13,14</sup>. Furthermore, many

of the cells reported thus far also use polymer binders to help with cell processing, and carbon additives to create sufficient electronic conduction in the cathode composite<sup>15,16</sup>.

The interdependence of cell performance measures and the lack of a basic reference system make it difficult to evaluate overall ASSB performance across different cell chemistries. What complicates this further is that many studies focus on demonstrating particular aspects of ASSBs, and the full cell performance is not always described by the same parameters. Therefore, reviews of the ASSB literature usually summarize the cell performance in extensive tables that list a varied selection of parameters<sup>17,18</sup>. Here, we analyse the ASSB literature in relation to minimalistic cells and quantify the target parameters in back-of-the-envelope-style calculations, thus highlighting the main goals for ASSB research.

## Literature analysis of model cells

Table 1 lists details of the ASSBs<sup>3–7,15,16,19–37</sup> included in our analysis and compiles the information on the cell components, cycling conditions and selected performance measures, such as specific capacity, C-rate (C), specific energy, specific power and energy efficiency. We include all ASSBs from the literature that allowed us to carry out a consistent full cell analysis. In some cases we selected representative examples, as the inclusion of all reports would have exceeded the scope of this analysis. Most of the cells included in our analysis are not optimized for energy and power, which the reader should bear in mind when interpreting the results. Although industry is in the process of developing optimized ASSBs, data currently available on these are insufficient for a complete analysis. We exclude cells with an indium anode, as this is not considered a viable AAM for practical applications due to its density and cost. We also exclude hybrid cells that use liquids or gels. Whenever available, we include data specified in the original reference. All remaining values are

<sup>1</sup>Institute of Physical Chemistry & Center for Materials Research, Justus-Liebig-University Giessen, Giessen, Germany. <sup>2</sup>Karlsruhe Institute of Technology, Institute for Applied Materials, Karlsruhe, Germany. <sup>3</sup>BASF SE, Ludwigshafen am Rhein, Germany. <sup>4</sup>Present address: Volkswagen AG, Group Research, Wolfsburg, Germany. <sup>5</sup>Present address: BMW Group, München, Germany. ✉e-mail: [felix.h.richter@phys.chemie.uni-giessen.de](mailto:felix.h.richter@phys.chemie.uni-giessen.de); [Juergen.Janek@phys.Chemie.uni-giessen.de](mailto:Juergen.Janek@phys.Chemie.uni-giessen.de)

**Table 1 | Comparison of battery composition of cell type 1 and cell type 2 with that of previously reported ASSB cells**

Reference	Cell composition				Temperature	
	Cathode composite			Solid electrolyte	Anode	T (°C)
	CAM	Coating	Carbon		AAM	
ASSBs with thiophosphate electrolyte						
Minimalistic cell						
Cell type 1	NCM622	–	–	$\beta$ -Li <sub>3</sub> PS <sub>4</sub>	Li	25
Cell type 2	NCM622	–	–	$\beta$ -Li <sub>3</sub> PS <sub>4</sub>	Li	25
Intercalation-type CAM and lithium metal						
Whiteley et al. <sup>19</sup>	NCM111	Al <sub>2</sub> O <sub>3</sub>	Super C65	Li <sub>10</sub> SiP <sub>2</sub> S <sub>12</sub>	Li	25
Zhang et al. <sup>20</sup>	LiCoO <sub>2</sub>	LiNbO <sub>3</sub>	–	Li <sub>10</sub> GeP <sub>2</sub> S <sub>12</sub> with LiH <sub>2</sub> PO <sub>4</sub> coating to Li	Li	25
Woo et al. <sup>21</sup>	LiCoO <sub>2</sub>	Al <sub>2</sub> O <sub>3</sub>	AB	Catholyte: Li <sub>3.15</sub> Ge <sub>0.15</sub> P <sub>0.85</sub> S <sub>4</sub> , separator: 77.5Li <sub>2</sub> S–22.5P <sub>2</sub> S <sub>5</sub>	Li	25
Xie et al. <sup>22</sup>	LiCoO <sub>2</sub>	LiNbO <sub>3</sub>	–	Catholyte: Li <sub>10</sub> GeP <sub>2</sub> S <sub>12</sub> , separator: Li <sub>3</sub> P <sub>1-x</sub> Sb <sub>x</sub> S <sub>4-2.5x</sub> O <sub>2.5x</sub>	Li	25
Ulissi et al. <sup>23</sup>	NCA	Li <sub>2</sub> ZrO <sub>3</sub>	Super C65	75Li <sub>2</sub> S–25P <sub>2</sub> S <sub>5</sub>	Li–C	25
Choi et al. <sup>24</sup>	NCM622	–	Super P	Li <sub>7</sub> P <sub>2</sub> S <sub>8</sub> I	Li	55
Intercalation-type CAM and graphite						
Nam et al. <sup>15</sup>	NCM622	LiNbO <sub>3</sub>	Graphite	Li <sub>6</sub> PS <sub>5</sub> Cl	Graphite	25
Nam et al. <sup>15</sup>	NCM622	LiNbO <sub>3</sub>	Graphite	Li <sub>6</sub> PS <sub>5</sub> Cl	Graphite	25
Yamamoto et al. <sup>25</sup>	NCM111	LiNbO <sub>3</sub>	Graphite	Li <sub>3</sub> PS <sub>4</sub> glass	Graphite	25
Sakuda et al. <sup>16</sup>	NCM111	LiNbO <sub>3</sub>	AB	75Li <sub>2</sub> S–25P <sub>2</sub> S <sub>5</sub>	Graphite	30
Kato et al. <sup>3</sup>	LiCoO <sub>2</sub>	LiNbO <sub>3</sub>	AB	Catholyte and separator: Li <sub>10</sub> GeP <sub>2</sub> S <sub>12</sub> , anolyte and separator: Li <sub>9.6</sub> P <sub>3</sub> S <sub>12</sub>	Graphite	25
Kato et al. <sup>26</sup>	LiCoO <sub>2</sub>	LiNbO <sub>3</sub>	AB	Catholyte: Li <sub>10</sub> GeP <sub>2</sub> S <sub>12</sub> , separator and anolyte: LiI–Li <sub>2</sub> S–P <sub>2</sub> S <sub>5</sub>	Graphite	25
Ito et al. <sup>27</sup>	NCA	Li <sub>2</sub> O–ZrO <sub>2</sub>	VGCF	80Li <sub>2</sub> S–20P <sub>2</sub> S <sub>5</sub>	Graphite	25
Kim et al. <sup>28</sup>	LiCoO <sub>2</sub>	LiNbO <sub>3</sub>	Super P	Li <sub>6</sub> PS <sub>5</sub> Cl	Graphite	30
Kraft et al. <sup>29</sup>	NCM622	–	–	Li <sub>6.6</sub> P <sub>0.4</sub> Ge <sub>0.6</sub> S <sub>9</sub> I	Li <sub>4</sub> Ti <sub>5</sub> O <sub>12</sub>	60
Conversion-type CAM and lithium metal						
Yamada et al. <sup>30</sup>	S	–	CNF	Li <sub>3</sub> PS <sub>4</sub> glass	Li	20
Yao et al. <sup>6</sup>	Co <sub>9</sub> S <sub>8</sub>	Li <sub>7</sub> P <sub>3</sub> S <sub>11</sub>	Super P	Catholyte: Li <sub>10</sub> GeP <sub>2</sub> S <sub>12</sub> , separator: 70Li <sub>2</sub> S–29P <sub>2</sub> S <sub>5</sub> –1P <sub>2</sub> O <sub>5</sub>	Li	25
Zhang et al. <sup>31</sup>	NiS–CNT	Li <sub>10</sub> GeP <sub>2</sub> S <sub>12</sub>	Super P	Catholyte: Li <sub>10</sub> GeP <sub>2</sub> S <sub>12</sub> , separator: 70Li <sub>2</sub> S–29P <sub>2</sub> S <sub>5</sub> –1P <sub>2</sub> O <sub>5</sub>	Li	25
ASSBs with oxide/phosphate electrolyte						
Yu et al. <sup>4</sup>	Li <sub>3</sub> V <sub>2</sub> (PO <sub>4</sub> ) <sub>3</sub>	Carbon	Super P	Li <sub>1.3</sub> Al <sub>0.3</sub> Ti <sub>1.7</sub> (PO <sub>4</sub> ) <sub>3</sub>	LiTi <sub>2</sub> (PO <sub>4</sub> ) <sub>3</sub>	30
Finsterbusch et al. <sup>5</sup>	LiCoO <sub>2</sub>	–	–	Li <sub>6.6</sub> La <sub>3</sub> Zr <sub>1.6</sub> Ta <sub>0.4</sub> O <sub>12</sub>	Li	100
ASSBs with inorganic and polymer electrolyte						
Chen et al. <sup>32</sup>	LiFePO <sub>4</sub>	–	In <sub>2</sub> O <sub>5</sub> Sn	Composite of PEO–LiTFSI and Al–Li <sub>6.75</sub> La <sub>3</sub> Zr <sub>1.75</sub> Ta <sub>0.25</sub> O <sub>12</sub>	Li	60
Park et al. <sup>33</sup>	NCM622	–	Super P	Composite of PBA–LiClO <sub>4</sub> and Li <sub>1.5</sub> Al <sub>0.5</sub> Ge <sub>1.5</sub> (PO <sub>4</sub> ) <sub>3</sub>	Li	55
Wakayama et al. <sup>34</sup>	LiCoO <sub>2</sub>	–	–	Catholyte: Li <sub>7</sub> La <sub>3</sub> Zr <sub>2</sub> O <sub>12</sub> , separator: PEO–LiTFSI	Li	50
Ates et al. <sup>35</sup>	NCM622	–	VGCF	Catholyte: $\beta$ -Li <sub>3</sub> PS <sub>4</sub> , separator: PEO–LiTFSI	Li	60
ASSBs with polymer electrolyte						
Hovington et al. <sup>7</sup>	LiFePO <sub>4</sub>	Carbon	AB	PEO–LiTFSI	Li	70
Porcarelli et al. <sup>36</sup>	LiFePO <sub>4</sub>	–	–	SI–PEO–LiTFSI	Li	70
Bouchet et al. <sup>37</sup>	LiFePO <sub>4</sub>	Carbon	C65	SI–PEO–LiTFSI	Li	80
Lithium-ion battery						
Panasonic LIB <sup>46</sup>	NCA	ND	ND	Liquid electrolyte	Graphite	25
Panasonic LIB, lithium-ion battery NCR18650B; CAM, cathode active material; NCM622, Li(Ni <sub>0.6</sub> Co <sub>0.2</sub> Mn <sub>0.2</sub> )O <sub>2</sub> ; NCM111, Li(Ni <sub>0.3</sub> Co <sub>0.3</sub> Mn <sub>0.3</sub> )O <sub>2</sub> ; NCA, Li(Ni <sub>0.8</sub> Co <sub>0.15</sub> Al <sub>0.05</sub> )O <sub>2</sub> ; AB, acetylene black; VGCF, vapour grown carbon fibres; CNF, carbon nanofibres; PEO, poly(ethylene oxide); PBA, poly(1,4-butylene adipate); SI, single ion; LiTFSI, lithium bis(trifluoromethanesulfonyl)imide (LiC <sub>4</sub> F <sub>9</sub> NO <sub>2</sub> S <sub>2</sub> ); AAM, anode active material; ND, no data available. For details, we refer to the corresponding literature sources. Additional information on cell dimension and composition is summarized in Supplementary Table 4, and on cell capacity, voltage and energy efficiency is in Supplementary Table 5.						

Panasonic LIB, lithium-ion battery NCR18650B; CAM, cathode active material; NCM622, Li(Ni<sub>0.6</sub>Co<sub>0.2</sub>Mn<sub>0.2</sub>)O<sub>2</sub>; NCM111, Li(Ni<sub>0.3</sub>Co<sub>0.3</sub>Mn<sub>0.3</sub>)O<sub>2</sub>; NCA, Li(Ni<sub>0.8</sub>Co<sub>0.15</sub>Al<sub>0.05</sub>)O<sub>2</sub>; AB, acetylene black; VGCF, vapour-grown carbon fibres; CNF, carbon nanofibres; PEO, poly(ethylene oxide); PBA, poly(1,4-butylene adipate); SI, single ion; LiTFSI, lithium bis(trifluoromethanesulfonyl)imide (LiC<sub>2</sub>F<sub>5</sub>NO<sub>2</sub>S<sub>2</sub>); AAM, anode active material; ND, no data available. For details, we refer to the corresponding literature sources. Additional information on cell dimension and composition is summarized in Supplementary Table 4, and on cell capacity, voltage and energy efficiency is in Supplementary Table 5.

calculated from the available parameters using the equations specified in Supplementary Table 1 and, if necessary, using approximations listed in Supplementary Tables 2 and 3. Additional

information on cell dimensions and composition is summarized in Supplementary Table 4, and on cell capacity, voltage and energy efficiency in Supplementary Table 5.

The literature analysis benefits from comparing with a minimalistic cell, which contains only the bare minimum of compounds and can be assembled by simple pelletization at ambient temperature. We chose to construct cells with lithium metal foil as AAM,  $\beta$ -Li<sub>3</sub>PS<sub>4</sub> (LPS) solid electrolyte and Li(Ni<sub>0.6</sub>Co<sub>0.2</sub>Mn<sub>0.2</sub>)O<sub>2</sub> (NCM) as CAM and did not use protective coatings, carbon additives and binders. It should be noted, however, that Li<sub>2</sub>CO<sub>3</sub> and LiOH impurities, stemming from synthesis and storage, may be present on the NCM surface and may influence cell performance<sup>38,39</sup>. We chose  $\beta$ -Li<sub>3</sub>PS<sub>4</sub> as the solid electrolyte as it forms a comparatively suitable interphase with lithium metal<sup>40,41</sup>. In addition, sufficient densification of thiophosphate solid electrolytes is achieved by uniaxial stress at ambient temperature<sup>42</sup>. Furthermore, good cycling performance of ASSBs was demonstrated using NCM and  $\beta$ -Li<sub>3</sub>PS<sub>4</sub> solid electrolyte in combination with an indium anode<sup>41,43</sup>. A detailed analysis of the cells can be found in Supplementary Figs. 1–9 and Supplementary Tables 6–8.

First, we focus on the initial cell performance. Typically, the obtainable cell energy depends on the power applied during cycling. Both are plotted in a Ragone-type graph<sup>44</sup> excluding the weight of current collectors and cell casing for ASSBs, as the research focus still lies on the cell chemistry before the casing of ASSBs can be optimized (Fig. 1). As indicated by the target region in the top-right corner of the Ragone diagram, an ideal ASSB shows both high specific energy and high specific power. The target region marks a cell with more than 250 Wh kg<sup>-1</sup> specific energy and a cycling rate of more than 1C, which is the performance of state-of-the-art lithium-ion battery technology (including cell casing)<sup>45,46</sup>. The corresponding Ragone diagram for the energy density and power density is shown in Supplementary Fig. 10, in which the target region marks more than 700 Wh l<sup>-1</sup> energy density and a cycling rate of more than 1C. Supplementary Fig. 11 also shows a corresponding plot of the area capacity against the current density.

Considering only the specific energy,  $E_m$ , obtained at ambient temperature, so far there are no ASSBs that reach the value of lithium-ion batteries. ASSBs with graphite AAM and thiophosphate solid electrolyte lead the field, achieving almost 200 Wh kg<sup>-1</sup> by either decreasing the thickness of the solid electrolyte separator down to 30  $\mu$ m with the doctor-blade method<sup>15</sup>, or by increasing the thickness of the cathode layer up to 600  $\mu$ m in the thick electrode configuration<sup>26</sup>. The specific energy of thiophosphate-based ASSBs with lithium metal has been rather modest at ambient temperature (<27 Wh kg<sup>-1</sup>). This is largely caused by the use of relatively thick lithium metal foils and solid electrolyte separators. Oxide/phosphate-based ASSBs show inferior specific energy compared with thiophosphate-based ASSBs, achieving up to 12 Wh kg<sup>-1</sup>. ASSBs containing polymer or composite electrolytes achieve higher specific energy up to 288 Wh kg<sup>-1</sup> using lithium and LiFePO<sub>4</sub> as active materials, but require elevated temperatures of 50 to 80 °C, at which the internal resistance of the cells is sufficiently low (Fig. 1b). Use of higher potential CAMs results in oxidative decomposition of the polymer electrolyte<sup>47</sup>. To circumvent this problem, cells using inorganic solid electrolyte in the cathode composite, and a polymer solid electrolyte separator, were developed, but most have comparatively modest specific energy at elevated temperature.

The cathode composite determines the maximum specific energy possible in the cell. It is hypothetically reached if no solid electrolyte separator and anode are considered, while assuming a cell voltage of the cathode composite against Li<sup>+</sup>/Li. Therefore, we introduce  $E_{m(\text{Ca})}$  as the hypothetical specific energy of the cathode composite, which we define as the cell energy normalized only to the cathode composite mass, while assuming a cell voltage against Li<sup>+</sup>/Li. This allows comparison of the performance of the cathode composite between different studies that is independent of the type and quantity of separator and anode material used in the respective study. The resulting literature analysis in Table 2 shows that the highest hypothetical specific energy of the cathode composite

achieved was about 400 Wh kg<sup>-1</sup> with an intercalation-type CAM and about 900 Wh kg<sup>-1</sup> with a conversion-type CAM at ambient temperature. However, comparison of solely the hypothetical specific energy of the cathode composite probably favours studies with a thinner cathode layer. Therefore, it is especially important to keep the applied layer thicknesses in mind as well and moving towards cells with a higher area capacity. This is emphasized by the observation that most studies achieve similar hypothetical specific energy in the cathode composite (300–400 Wh kg<sup>-1</sup>), indicating that the large spread of the cell-specific energy observed in Fig. 1 mostly originates simply from variations in the applied layer thicknesses (Fig. 2). Thus, the hypothetical specific energy is especially helpful when comparing model cell systems such as these. Similarly, the hypothetical energy density  $E_{V(\text{Ca})}$  can be calculated and compared.

Additionally, the area capacity  $Q_A$  (cell capacity divided by cell cross-sectional area) also needs to be high, as this is necessary to achieve cells of sufficient size. While most studies achieve up to 2 mAh cm<sup>-2</sup>, some have demonstrated up to 14 mAh cm<sup>-2</sup> (see Table 2). Correspondingly, the area energy  $E_A$  can be compared as well. It is obtained by dividing the energy of the cell by the cell cross-sectional area. Most studies achieve up to 75 Wh m<sup>-2</sup>. Some have demonstrated up to 574 Wh m<sup>-2</sup>. However, it is vital that the hypothetical specific energy and the area energy are increased simultaneously, as the former is a specific property of the cathode composite, while the latter is indicative of cell size.

Whereas the specific energy also depends on the density of the materials used in the cell, the energy density  $E_V$  is solely dependent on the layer thicknesses within the cell. While the hypothetical energy density of the cathode composite, analogous to the hypothetical specific energy, determines the maximum achievable energy density, the layer thicknesses of the anode and separator simply need to be minimized. Free-standing lithium foil as thin as 20  $\mu$ m is currently available commercially and solid electrolyte layers of less than 50  $\mu$ m have already been demonstrated (Fig. 2 and Supplementary Table 4)<sup>15,31,48</sup>. Due to the low density of lithium, the impact of the lithium foil thickness on energy density is larger than on the specific energy of a cell. Nonetheless, the trends discussed for the specific energy also apply when comparing energy density (Supplementary Fig. 10).

When using solid electrolytes with lithium transfer number close to unity and high ionic conductivity, ASSBs with intercalation-type electrodes can provide higher power than lithium-ion batteries normalized to the CAM content<sup>3</sup>. More than 1,000 W kg<sup>-1</sup> specific power,  $P_m$ , was demonstrated, albeit at comparatively low specific energy using a graphite anode. Polymer-based ASSBs struggle to achieve similar specific power, even at elevated temperatures. Generally, specific power depends on the cell potential, area density (mass of cell divided by cell area) and current density (see Supplementary Table 1). As the cell potential changes during cycling, specific power at any given point during discharge is dependent on the state of charge. Therefore, we plot the average specific power during discharge at constant current density in the Ragone diagram.

Sometimes, the C-rate (specific current of CAM divided by specific capacity of CAM) is stated instead of the current density,  $j$  (current divided by cell area). Both parameters are important descriptors, but for different aspects. Whereas the current density through the cross-section area of the cell is directly comparable between cells, the C-rate also depends on the cell capacity obtained, which varies between studies. For example, a cell with smaller area capacity requires a lower current density to achieve the same C-rate. Consequently, the C-rate remains ambiguous if the capacity to which it refers is not explicit. Therefore, current density should be preferred as the value stated in the experimental section. The C-rate may be reported in the results section on the basis of the obtained capacity. It is listed as such in Table 2.

Current density is a critical parameter to evaluate the occurrence of a short-circuit due to lithium penetration of the solid electrolyte

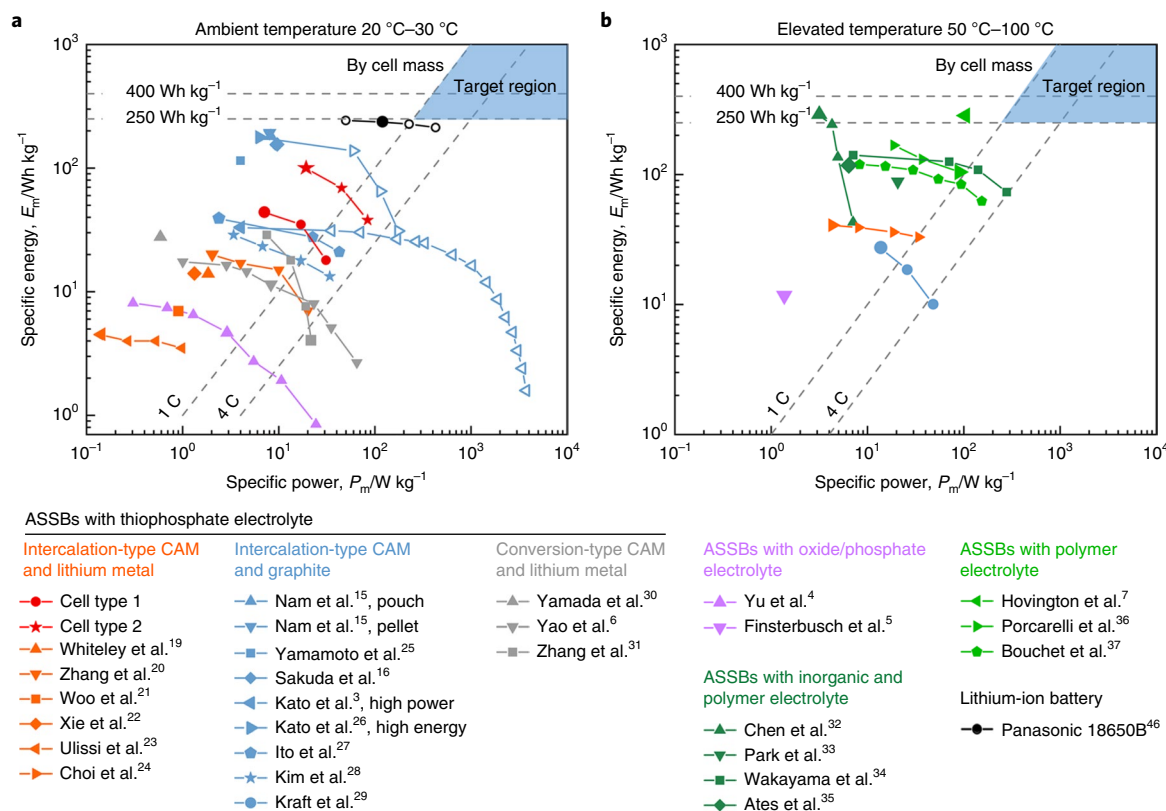


**Fig. 1 | Ragone plots for cells cycled at different temperatures. a,b**, Ambient (20–30 °C) (a) and elevated (50–100 °C) (b) temperature. Dashed lines indicate targets for specific energy and C-rate. The area in blue depicts the target region where both energy and rate performance excel. The specific energy shown here is the energy delivered by the cell during discharge, normalized to the cell mass. The specific power is the average power delivered by the cell during discharge, normalized to the cell mass. For ASSBs, the weight of the cell casing and current collectors is omitted here. Literature data for the performance comparison of cells were obtained as indicated in Table 1. ASSBs with thiophosphate solid electrolyte, intercalation-type CAM and lithium metal (orange); ASSBs with thiophosphate solid electrolyte, intercalation-type CAM and graphite (blue); ASSBs with thiophosphate solid electrolyte, conversion-type CAM and lithium metal (grey); ASSBs with polymer electrolyte (light green); ASSBs with inorganic and polymer electrolyte (dark green); and ASSBs with oxide/phosphate electrolyte (violet) and a commercial lithium-ion battery (black) are compared. Our own data for the Ragone plot were obtained from the discharge curves of cell type 1 and cell type 2 cycled at 25 °C (red). Large symbols indicate conditions under which prolonged cycling was demonstrated and correspond to data detailed in Table 1. Small symbols indicate data points of the corresponding rate test if available. Filled symbols indicate data of cells that were charged and discharged at equal current density. Empty symbols indicate cycling data in which the rate test was only applied to discharge, whereas charging was carried out at lower current.

separator. Whereas a current density exceeding  $20 \text{ mA cm}^{-2}$  has been demonstrated with graphite-type ASSBs<sup>3</sup>, applying a prolonged current density of  $1 \text{ mA cm}^{-2}$  and more with a lithium metal anode is usually accompanied by internal shorting of the cell, often referred to as lithium dendrite formation. Nonetheless, prolonged cycling of an ASSB with lithium metal anode at  $1.27 \text{ mA cm}^{-2}$ , and up to  $12.7 \text{ mA cm}^{-2}$  in a rate test, has been demonstrated at ambient temperature. In another study, the critical current density at which the short-circuit occurs in LPS was increased from  $0.7 \text{ mA cm}^{-2}$  to  $2.0 \text{ mA cm}^{-2}$  by introducing a LiF-rich solid electrolyte interphase between  $\text{Li}_3\text{PS}_4$  and lithium<sup>49</sup>. The C-rate and specific current (current per gram of CAM) are most important for studies investigating the CAM and cathode composite performance. However, this requires that CAM-related processes dominate the factors limiting cell performance.

The internal resistance  $R$  influences the overpotential,  $\eta$ , energy efficiency and power capability of the cell during cycling. It can be directly compared between cells, when noted as area-normalized resistance in  $\Omega \text{ cm}^2$ , simply using the cross-section area of the cell. However, care needs to be taken as it is dependent on the state of charge. As little as  $14 \Omega \text{ cm}^2$  internal resistance at ambient temperature was demonstrated for an ASSB with graphite AAM,

thiophosphate solid electrolyte and  $\text{LiCoO}_2$ <sup>3</sup>. Via Ohm's law, the overpotential of the cell is directly linked with the applied current density and the internal resistance. A substantial overvoltage in the cell leads to a large discrepancy between the energy required for charge and that released during discharge.

The energy efficiency of the charge–discharge sequence,  $\Phi_{E(\text{ch-dis})}$  (energy of  $n$ th discharge divided by energy of  $n$ th charge), needs to be maximized in the interests of reducing energy loss during battery cycling. It is the product of the corresponding Coulomb efficiency,  $\Phi_{Q(\text{ch-dis})}$  (capacity of  $n$ th discharge divided by capacity of  $n$ th charge), and voltage efficiency,  $\Phi_{V(\text{ch-dis})}$  (average voltage of  $n$ th discharge divided by average voltage of  $n$ th charge). As the Coulomb efficiency must necessarily be high to allow long-term cycling of a secondary battery, the voltage efficiency is usually the critical factor that determines the energy efficiency of each cycle (Supplementary Fig. 12).

Estimating the energy efficiency of the surveyed literature was often only possible by extracting the average charge and discharge voltages from the voltage profiles presented. Cells with intercalation-type CAM mostly exceed 90% energy efficiency from the 2nd cycle onwards, and so far surpass that of cells with conversion-type CAM (Table 2 and Supplementary Table 5). This is in part explained by the higher cell voltages of the intercalation-type CAMs, as any

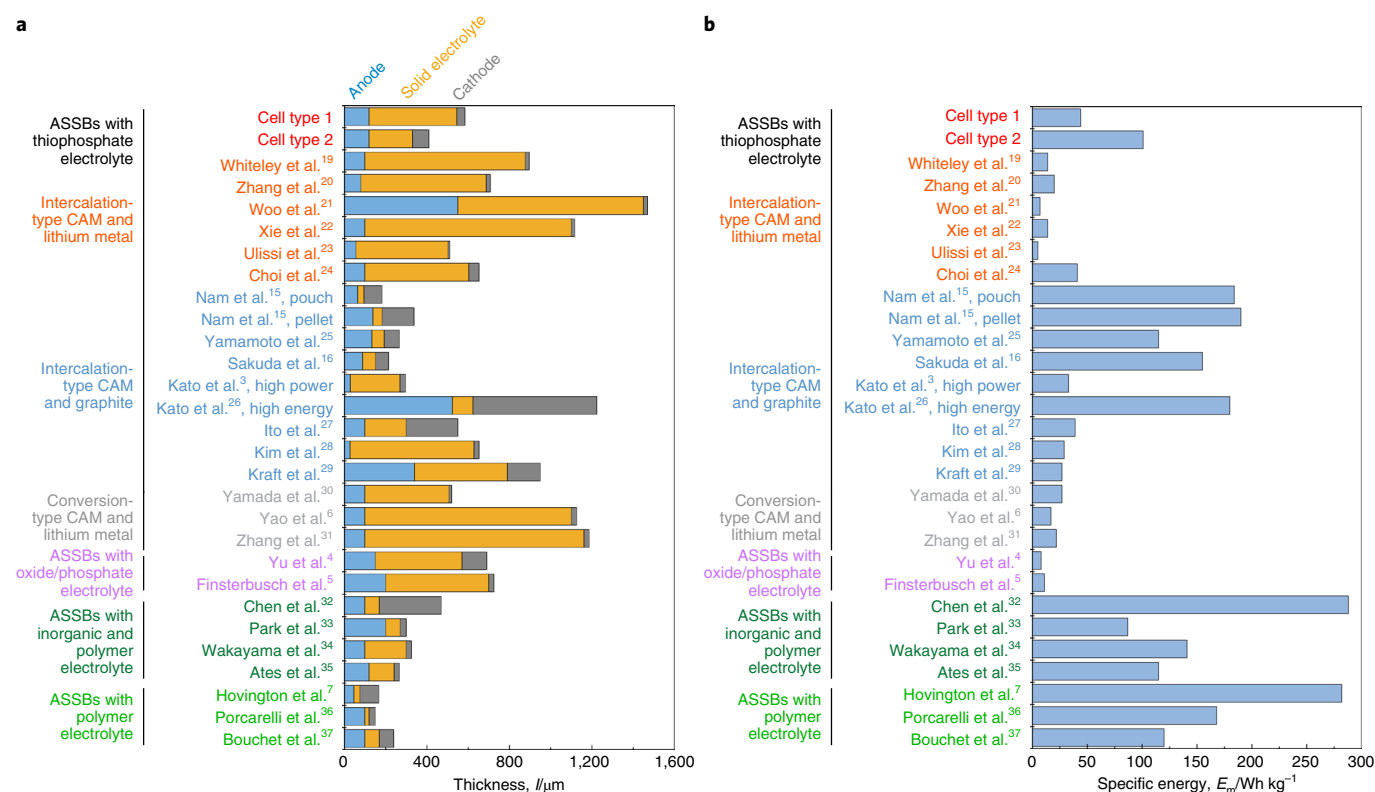


**Fig. 2 | Relationship between layer thicknesses and specific energies of analysed ASSBs. a, b**, Representation of layer thicknesses of ASSBs (**a**) and the corresponding cell-specific energies as histograms (**b**). Corresponding data are available in Supplementary Tables 2 and 4.

overvoltage will affect energy efficiency less for cells operating at higher voltage. Analysis of the minimalistic cells shows that voltage efficiency decreases during cycling, indicating an increase in overpotential of the cell (Supplementary Fig. 12).

When it comes to battery cycling analysis, energy retention,  $\Phi_{E(\text{dis})}$  (energy of discharge of  $n$ th cycle divided by energy of discharge of first cycle), is the key parameter as it covers both contributions to energy loss: capacity loss and overpotential increase. Generally, capacity loss is the dominant factor, with the additional influence of the change in overpotential typically having less effect on energy retention (Supplementary Fig. 12). Therefore, cell ageing is often reported by plotting capacity as a function of the cycle number, as shown in Supplementary Fig. 13. Additionally, the development of the specific energy of the cell during cycling, as plotted in Fig. 3a, also indicates high and low specific energy cells and allows the comparison of cells with different types of CAM in one diagram.

Still, the number of cycles tested and the area energy delivered by the tested cell per cycle vary strongly between studies. On the cell level, the goal is to maintain high specific energy per cycle while delivering greater area energy. Hence, Fig. 3b plots the specific energy of cycle  $n$  against the area energy delivered during all discharges up to cycle  $n$  (delivered area energy  $\Sigma_n E_A$ ), which is more indicative of the overall cell performance. Comparison of the two types of plots shows that a low cycle number can still translate into a substantial area-normalized energy being delivered, depending on the area capacity<sup>26</sup>. The total delivered area energy ( $\Sigma_{\text{tot}} E_A$ ) over all cycles shown in the original references is listed in Table 2.

In terms of energy retention during cycling at ambient temperature, ASSBs with a protected lithium anode, thiophosphate-based solid electrolyte and intercalation-type CAM<sup>20</sup>, as well as with conversion-type CAM<sup>6</sup>, excel, achieving  $1.26 \text{ Wh cm}^{-2}$  and  $1.93 \text{ Wh cm}^{-2}$ , respectively, for delivered area energy ( $\Sigma_{\text{tot}} E_A$ ) with little capacity loss over 500 and 1,000 cycles, respectively. These

examples demonstrate the importance of protective layers in preventing battery degradation. Pretreatment of lithium metal with 80 wt%  $\text{H}_3\text{PO}_4$  solution to form a  $\text{LiH}_2\text{PO}_4$  protective layer was shown to improve the energy retention of the lithium metal anode<sup>20</sup>. Similarly, the addition of 1%  $\text{P}_2\text{O}_5$  to  $\text{Li}_2\text{S}-\text{P}_2\text{S}_5$  glass stabilized the lithium–thiophosphate interface over 1,000 cycles<sup>6</sup>. Amongst the high specific energy cells at ambient temperature, cells with  $\text{LiNbO}_3$ -coated  $\text{LiCoO}_2$  and graphite show the most stable cycling<sup>26</sup>. At elevated temperatures, the energy retention of cells with polymer electrolytes is excellent with  $\text{LiFePO}_4$  and lithium, achieving  $8.45 \text{ Wh cm}^{-2}$  delivered area energy over 1,400 cycles<sup>7</sup>. Also, the  $\text{Li}_{0.6}\text{La}_{0.3}\text{Zr}_{1.6}\text{Ta}_{0.4}\text{O}_{12}$ -based cell showed excellent energy retention with  $\text{LiCoO}_2$  and lithium at  $100^\circ\text{C}$  (ref. <sup>5</sup>). On the cathode side,  $\text{LiNbO}_3$  is a suitable coating for  $\text{LiCoO}_2$ , allowing excellent energy retention, as demonstrated in cells with thiophosphate-based solid electrolytes and lithium metal<sup>20</sup> as well as graphite AAM<sup>3,26</sup>.

There is as yet no singular set of parameters commonly used for the characterization of ASSBs and their performance across different studies. On the basis of the fundamental definitions and equations describing battery performance (Supplementary Table 1), we identified a practical set of parameters that can be directly compared, and from which all others can be calculated. These are listed and commented on in Table 3. Supplementary Data 1 demonstrates how the performance measures can be calculated from this set of parameters by modifying the values of the input parameters as described in the Methods.

Amongst the less commonly reported values, the average voltage and its development during cycling is most critical, as without it neither specific energy nor specific power can be calculated from the capacity alone. Impedance measurements are required to evaluate solid electrolyte ionic conductivity and charge transfer resistances of the electrodes. Cycling performance is also reported inconsistently, varying over a large range of cycles, time, current density and



**Table 2 | Comparison of battery performance of cell type 1 and cell type 2 with previously reported ASSB cells**

Reference	Results of initial cycle(s)								Cycling test				
	$j_1^a$ (mA m <sup>-2</sup> )	$q_{dis}$ (mAh g <sup>-1</sup> )	C-rate (h <sup>-1</sup> )	$E_m$ (Wh kg <sup>-1</sup> )	$E_{m(Ca)}^b$ (Wh kg <sup>-1</sup> )	$Q_A$ (mAh cm <sup>-2</sup> )	$E_A$ (Wh m <sup>-2</sup> )	$\Phi_{E(ch-dis)}^c$ (%)	$j_2^a$ (mA cm <sup>-2</sup> )	$P_m$ (W kg <sup>-1</sup> )	$j_3^a$ (mA cm <sup>-2</sup> )	Cycles (in total)	$\Sigma_{tot} E_A$ (Wh cm <sup>-2</sup> )
ASSBs with thiophosphate electrolyte													
Minimalistic cell													
Cell type 1	0.178	128	0.16	44	328	1.14	42	92	0.89	30.9	0.178	211	0.56
Cell type 2	0.356	107	0.19	100	276	1.91	71	91	1.78	84.0	0.356	230	0.93
Intercalation-type CAM and lithium metal													
Whiteley et al. <sup>19</sup>	0.082	125 <sup>d</sup>	0.13	14 <sup>e</sup>	308 <sup>e</sup>	0.64 <sup>d</sup>	23 <sup>e</sup>	95 <sup>d</sup>	0.082	1.8 <sup>e</sup>	0.082	75	0.17
Zhang et al. <sup>20</sup>	0.075 <sup>e</sup>	133	0.1	20 <sup>d,e</sup>	308 <sup>e</sup>	0.83	28 <sup>d,e</sup>	98 <sup>d</sup>	0.75	20.0 <sup>e</sup>	0.075 <sup>e</sup>	500	1.26
Woo et al. <sup>21</sup>	0.045	121 <sup>d</sup>	0.13	7 <sup>d</sup>	175 <sup>d</sup>	0.46 <sup>d</sup>	17 <sup>d</sup>	91 <sup>d</sup>	0.045	0.9 <sup>d</sup>	0.045	25	0.03
Xie et al. <sup>22</sup>	0.066	134	0.09	14 <sup>e</sup>	411 <sup>e</sup>	0.79	26 <sup>e</sup>	97 <sup>d</sup>	0.066	1.3 <sup>e</sup>	0.066	50	0.12
Ulissi et al. <sup>23</sup>	0.004	100	0.03	5 <sup>d</sup>	197 <sup>d</sup>	0.14	5 <sup>d</sup>	91 <sup>d</sup>	0.032	1.0 <sup>d</sup>	0.004	100	0.03
Choi et al. <sup>24</sup>	0.12	170	0.1	42	440	1.19	44	93	1.2	34.0	0.12	40	0.15
Intercalation-type CAM and graphite													
Nam et al. <sup>15</sup>	0.147 <sup>e</sup>	121	0.04	190 <sup>f</sup>	377	3.55	136	96 <sup>d</sup>	0.147	7.9 <sup>e,f</sup>	0.147 <sup>e</sup>	19	0.25
Nam et al. <sup>15</sup>	0.072 <sup>e</sup>	112	0.04	184 <sup>f</sup>	350	1.60	72	97 <sup>d</sup>	0.072	8.2 <sup>e,f</sup>	0.072 <sup>e</sup>	13	0.07
Yamamoto et al. <sup>25</sup>	0.064	116	0.03	115	319	1.85	65	59 <sup>d</sup>	0.064	4.0	0.064	ND	ND
Sakuda et al. <sup>16</sup>	0.064	114	0.06	155	397 <sup>e</sup>	1.08	56	92 <sup>d</sup>	0.064	9.2 <sup>e</sup>	0.064	15	0.06
Kato et al. <sup>3</sup>	0.067	114 <sup>d</sup>	0.12	33	266 <sup>e</sup>	0.55 <sup>d</sup>	21	97 <sup>d</sup>	91.31	3,745.0 <sup>d</sup>	0.067	30	0.06
Kato et al. <sup>26</sup>	0.50	123	0.04	180	311 <sup>e</sup>	14.18	574	98 <sup>d</sup>	20.0	175.7 <sup>e</sup>	0.50	10	0.53
Ito et al. <sup>27</sup>	0.05	121 <sup>d</sup>	0.06	39 <sup>d</sup>	268 <sup>d</sup>	0.82 <sup>d</sup>	29 <sup>d</sup>	ND	1.0	42.6 <sup>d</sup>	0.05	100	0.28
Kim et al. <sup>28</sup>	0.14	119	0.1	29 <sup>e</sup>	388 <sup>e</sup>	1.19	44 <sup>e</sup>	84 <sup>d</sup>	1.4	33.9 <sup>e</sup>	0.14	ND	ND
Kraft et al. <sup>29</sup>	1.71	99	0.51	27 <sup>d</sup>	249 <sup>d,e</sup>	3.40	71 <sup>d</sup>	89 <sup>d</sup>	6.84	48.0 <sup>d</sup>	1.71	50	0.40
Conversion-type CAM and lithium metal													
Yamada et al. <sup>30</sup>	0.025	1,600	0.02	27 <sup>d,e</sup>	912 <sup>d,e</sup>	0.96	22 <sup>d,e</sup>	84 <sup>d</sup>	0.025	0.6 <sup>d,e</sup>	0.025	10	0.02
Yao et al. <sup>6</sup>	0.13	647	0.06	17 <sup>d,e</sup>	386	2.33	33 <sup>d,e</sup>	78 <sup>d</sup>	12.73	64.9 <sup>d,e</sup>	1.27	1,000	1.93
Zhang et al. <sup>31</sup>	0.57	550	0.18	22 <sup>d,e</sup>	359 <sup>d,e</sup>	3.14	46 <sup>d,e</sup>	71 <sup>d</sup>	5.73	28.8 <sup>d,e</sup>	5.73	150	0.18
ASSBs with oxide/phosphate electrolyte													
Yu et al. <sup>4</sup>	0.043	102	0.04	8	166 <sup>e</sup>	1.01	11	ND	4.29	24.4	0.43	500	0.44
Finsterbusch et al. <sup>5</sup>	0.10	118	0.12	11 <sup>e</sup>	232 <sup>e</sup>	0.83	32 <sup>e</sup>	92	0.1	1.4 <sup>e</sup>	0.10	70	0.16
ASSBs with inorganic and polymer electrolyte													
Chen et al. <sup>32</sup>	0.10	155	0.01	288 <sup>e</sup>	362 <sup>e</sup>	9.42	294 <sup>e</sup>	81 <sup>d</sup>	0.3	7.1 <sup>e</sup>	0.10	11	0.29
Park et al. <sup>33</sup>	0.24 <sup>e</sup>	170	0.24	87 <sup>e</sup>	377 <sup>e</sup>	1.02	37 <sup>e</sup>	95 <sup>f</sup>	0.24	21 <sup>e</sup>	0.24 <sup>e</sup>	100	0.33
Wakayama et al. <sup>34</sup>	0.08 <sup>e</sup>	136	0.05	141 <sup>e</sup>	471 <sup>e</sup>	1.59	59 <sup>e</sup>	95	3.08	278.8 <sup>e</sup>	0.08 <sup>e</sup>	ND	ND
Ates et al. <sup>35</sup>	0.06	136	0.06	115 <sup>e</sup>	341 <sup>e</sup>	1.01	39 <sup>e</sup>	95	0.06	6.3 <sup>e</sup>	0.06	50	0.23
ASSBs with polymer electrolyte													
Hovington et al. <sup>7</sup>	0.81 <sup>e</sup>	158	0.36	282 <sup>e</sup>	364 <sup>e</sup>	2.32	73 <sup>e</sup>	87 <sup>d</sup>	0.81	100.3 <sup>e</sup>	0.81 <sup>e</sup>	1,400	8.45
Porcarelli et al. <sup>36</sup>	0.09 <sup>e</sup>	152	0.11	168 <sup>e</sup>	336 <sup>e</sup>	0.79	25 <sup>e</sup>	ND	0.43	91.4 <sup>e</sup>	0.43	300	0.43
Bouchet et al. <sup>37</sup>	0.05 <sup>e</sup>	162	0.07	120 <sup>e</sup>	329 <sup>e</sup>	0.78	26 <sup>e</sup>	ND	1.6	153.6 <sup>e</sup>	0.05 <sup>e</sup>	ND	ND
Lithium-ion battery													
Panasonic LIB <sup>46</sup>	ND	ND	0.2	243	ND	ND	ND	ND	ND	50	ND	ND	ND

Panasonic LIB, lithium-ion battery NCR18650B (specific energy and specific power values also take cell casing into account); ND, no data available. Unless indicated otherwise, values represent the performance of the initial discharge cycle(s) and were either specified or calculated (Supplementary Table 1) entirely from values specified in the respective reference. <sup>a</sup> $j_1$ : lowest available current density;  $j_2$ : highest available current density;  $j_3$ : current density at which prolonged cycling was demonstrated. <sup>b</sup>Hypothetical specific energy of the cathode composite  $E_{m(Ca)}$  is based solely on the cathode composite weight and assumes that the anode potential is equivalent to Li<sup>+</sup>/Li. For graphite 0.1 V, for Li<sub>2</sub>Ti<sub>3</sub>O<sub>7</sub> 1.5 V and for LiTi<sub>2</sub>(PO<sub>4</sub>)<sub>3</sub> 2.5 V average potential versus Li<sup>+</sup>/Li was assumed. <sup>c</sup>The energy efficiency of the charge-discharge sequence was obtained from the second cycle, except for Whiteley et al.<sup>19</sup>, Yamamoto et al.<sup>25</sup>, Kraft et al.<sup>29</sup> and Yamada et al.<sup>30</sup>, where it was obtained from the first cycle, and Woo et al.<sup>21</sup>, where it was obtained from the third cycle. <sup>d</sup>Not all data were available as number values in the respective reference. Data were extracted from figures in the respective reference, as detailed in Supplementary Tables 2 and 3. <sup>e</sup>Not all data were available in the respective references to calculate these values. Approximations had to be made as detailed in Supplementary Tables 2 and 3. <sup>f</sup>Weight of cell also includes weight of current collectors.

discharge capacity. Whenever possible, the area-normalized energy delivered until 80% of the original specific energy is reached, as well as the retained specific capacity after 100 cycles, should be reported. Correlating energy retention during cycling with the development of internal resistance may provide further insights into the

degradation mechanism. A plot of the resistances obtained from impedance analysis against the cycle number can help to identify the cause for an increase in overpotential that may occur during cycling<sup>27</sup>. However, care needs to be taken in this analysis, as the internal resistance is also dependent on the state of charge.

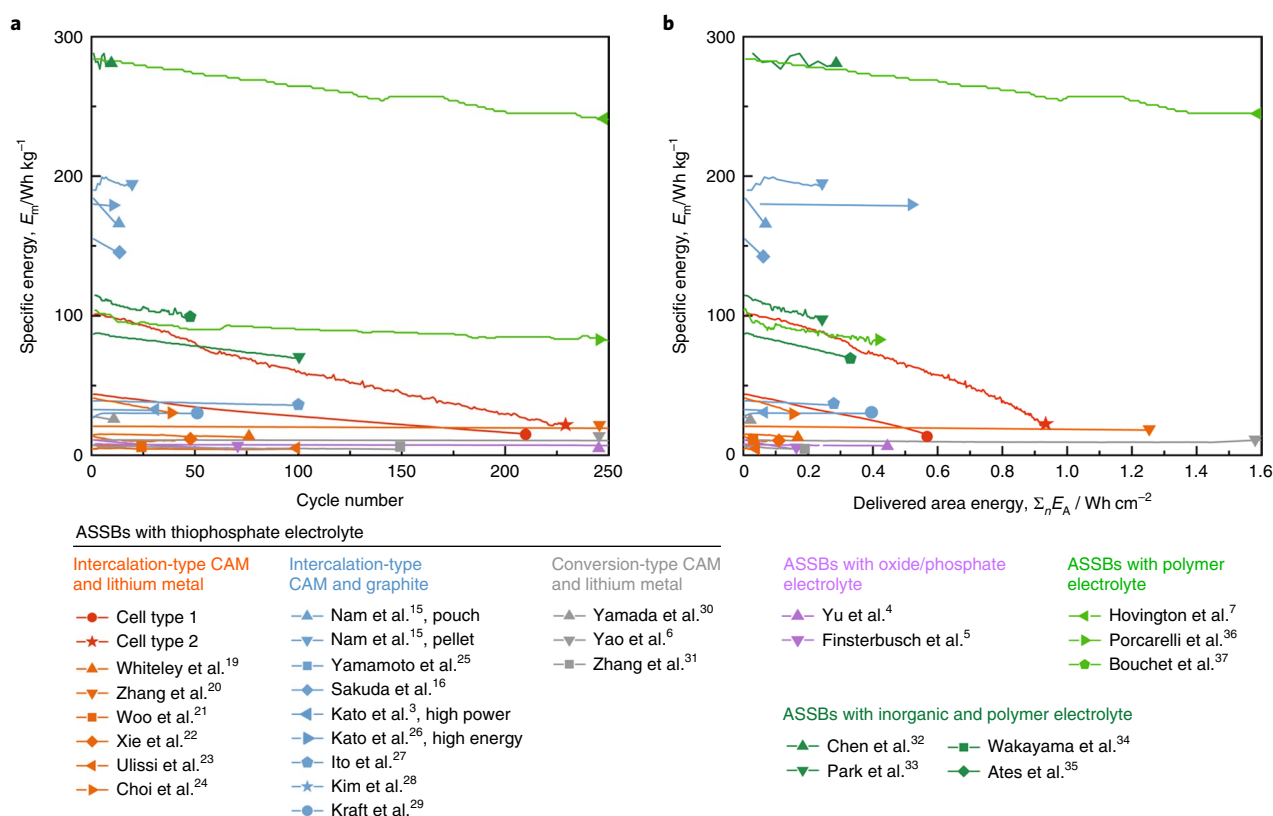


**Fig. 3 | Cycling results of analysed ASSBs. a, b**, Specific energy per cycle versus cycle number (**a**) and specific energy per cycle versus the sum of cell area-normalized energies (**b**) delivered by the cell during all discharges up to the respective cycle number. The applied current densities and obtained specific energies of the first discharge are detailed in Table 2. Because data for the development of the overpotential during cycling are mostly not available, we solely applied the capacity loss proportionally to the initial specific energy of the respective cell. This means assuming that the overpotential remains constant during cycling, which is acceptable here, as energy retention is usually dominated by capacity retention. To ensure clarity of the images, the cycling results extending beyond the x axis scale were truncated at 250 cycles or 1.6 Wh cm<sup>-2</sup>, respectively. Each line is composed of as many data points as numbers of cycles available for each cell. Individual points were omitted for clarity. Symbol meanings are the same as in Fig. 1. The sole purpose of the symbol at the end of each line is as a cell identifier.

## Performance prediction

Estimating cell performance measures on the basis of idealized assumptions is helpful to specify targets for research, while maintaining all parameters within reasonable margins. For example, increasing the CAM fraction in the cell is suitable to achieve higher energy density. However, this inherently means that the current density needs to be increased to maintain a high C-rate, requiring lower internal resistance of the cell. Hence, the cell performance and cell requirements can simply be estimated for any cell system using the fundamental equations for the specific energy, energy density, specific power, energy efficiency and Ohm's law (Supplementary Table 1). Several examples of these back-of-the-envelope-style calculations of cell performance are given in Supplementary Data 2. For the purposes of simplification, the internal resistance is assumed to be independent of the state of charge and the corresponding overvoltage applied equally to charge and discharge. Minority components, such as polymer binder and conducting carbon, are omitted in the following thought experiments. Three examples are described here. The corresponding boundary conditions and input parameters are discussed in Supplementary Table 9.

Example 1 in Supplementary Data 2 describes variants of an ASSB with lithium, thiophosphate solid electrolyte and NCM with an area capacity of 5 mAh cm<sup>-2</sup> by variable layer thicknesses and weight fraction of CAM. To have a chance to exceed 400 Wh kg<sup>-1</sup> energy density with NCM, the specific discharge capacity needs to exceed 170 mAh g<sub>CAM</sub><sup>-1</sup> in an 89-μm-thick cathode composite

containing 85 wt% CAM, in a cell with 40 μm thiophosphate solid electrolyte separator and 20 μm lithium metal anode. Also, the maximum allowed internal resistance can be calculated. To achieve a cell with 5 mAh cm<sup>-2</sup>, 90% energy efficiency and a cycling rate of 1C, the internal resistance must be less than 40 Ω cm<sup>2</sup>. Varying the lithium thickness of said cell demonstrates its substantial influence on the energy density. The same argument is valid for varying the solid electrolyte thickness. Without solid electrolyte and lithium metal, the hypothetical energy density of the composite cathode is obtained, which corresponds to the maximum attainable value with the respective cathode composite.

Following the same procedure, lithium and LiNi<sub>0.5</sub>Mn<sub>1.5</sub>O<sub>4</sub> (LNMO, example 2 in Supplementary Data 2) as well as lithium and Li<sub>2</sub>S (example 3 in Supplementary Data 2) cells were evaluated. While the high potential of LNMO allows for higher internal resistance of the cell (<49 Ω cm<sup>2</sup>) at similar specific energy, the conversion-type ASSBs promise to substantially increase specific energy, but require much lower internal resistance. With the assumed limitation of 5 mAh cm<sup>-2</sup> (see Supplementary Table 9), a lithium-sulfur cell can reach about 700 Wh kg<sup>-1</sup> if the internal resistance is below 23 Ω cm<sup>2</sup> (assuming: 20 μm lithium foil, 40 μm thiophosphate solid electrolyte, 31 μm cathode composite, 70 wt% sulfur in the cathode composite, 90% energy efficiency and a 1C rate).

For a general comparison of ASSBs, we calculate the maximum allowed internal resistance and achievable specific energy (Supplementary Data 3) for each CAM (NCM, LNMO, Li<sub>2</sub>S) and

**Table 3 | A set of parameters necessary for an overall characterization of battery performance**

Parameter	Frequency of reporting and parameter description
Cell components	Widely reported; describes the composition.
Cell area, $A$	Mostly reported; indicates the size of the cell.
Layer mass, $m$ , or area density, $\rho_A$	Mostly reported; required to calculate specific energy and specific power. Area density is to be preferred over the absolute layer mass used in the experiment as it is directly comparable between cells of different area.
Layer thickness, $l$	Often reported; required to calculate energy density and power density. Useful to directly compare different cell types and sizes of cells.
Applied pressure, $p$	Often reported; important for cell preparation and cycling conditions.
Temperature, $T$	Widely reported; important for cycling conditions, as it influences the internal resistance.
Current, $I$ , or current density, $j$	Mostly reported; indicates conditions of cycling. To be preferred over the C-rate as it is independent of cell design and CAM specific capacity.
Average voltage, $U$	Rarely reported as a value; it is mostly available from the charge-discharge curves, but very cumbersome to extract for the reader. It should always be reported as it is required to calculate energy, power and energy efficiency. Its development over time contains information on cell degradation.
Specific capacity, $q$	Mostly reported for charge and discharge; sometimes only available from a graph.
Internal resistance, $R$	Although the ionic conductivity of the solid electrolyte is widely reported, the charge transfer resistances are less analysed and the internal resistance of ASSBs is often only available from the impedance plots. If possible, the resistances of the solid electrolyte separator and the charge transfer processes at anode and cathode are to be distinguished. Its development over time contains information on cell degradation and can be placed in context with the development of the overvoltage during cycling.
Rate test	Inconsistently reported; the specific energy at a current density of $0.1 \text{ mA cm}^{-2}$ and a rate test to indicate power performance should be reported.
Energy retention	Inconsistently reported; mostly demonstrated as plots of capacity versus cycle number. Additionally, a plot of the specific energy against the delivered area energy of the cell allows a more general comparison between cells. As values, the energy retention after 100 cycles and the delivered area energy (in $\text{Wh cm}^{-2}$ ) until 80% of the original specific energy remains can be stated.

solid electrolyte (PEO–LiTFSI,  $\text{Li}_6\text{PS}_5\text{Cl}$ ,  $\text{Li}_7\text{La}_3\text{Zr}_2\text{O}_{12}$ ) combination, dependent on the area capacity ( $1\text{--}10 \text{ mAh cm}^{-2}$ ), while maintaining a 1C rate and 90% energy efficiency. We assume the theoretical capacity for each CAM and that all cells contain a 20- $\mu\text{m}$  lithium metal foil anode. In the input parameters, we vary the volume fraction of CAM in the cathode composite (25 vol%, 50 vol%, 75 vol%), separator thickness (200  $\mu\text{m}$ , 50  $\mu\text{m}$ , 20  $\mu\text{m}$ ) and the use of current collectors (15  $\mu\text{m}$  aluminium, 15  $\mu\text{m}$  copper). Figure 4 shows the results. The smaller the internal resistance needs to be, the more challenging it is to develop such a system. Supplementary Fig. 14 plots the required current density against the specific energy following the same analysis.

For example, viewing the data in Fig. 4 shows that at a separator thickness of 200  $\mu\text{m}$  the lower cell voltage conversion-type systems are at a disadvantage to intercalation-type systems with higher cell voltage. Lower internal resistance and higher current density must be achieved to obtain the same specific energy and cycling performance. Most ASSBs to date use even thicker separators than this, which may explain the superior performance of ASSBs with intercalation-type CAMs observed so far (Fig. 1).

At 50- $\mu\text{m}$  separator thickness, it depends on the density of the solid electrolyte as to whether the resistance advantage lies with intercalation- or conversion-type cells. Exceptionally high specific energy beyond  $500 \text{ Wh kg}^{-1}$  can only be achieved with the conversion-type systems. Regarding the required current density, the advantage of conversion-type cells demonstrates itself already at 50- $\mu\text{m}$  separator thickness (Supplementary Fig. 14). Likewise, higher volume fraction of CAM in the cathode composite benefits conversion-type systems, such as Li–S ASSBs.

With exceptionally thin (20  $\mu\text{m}$ ) and low-density separators (PEO–LiTFSI), conversion systems offer a substantial advantage over intercalation-type cells to achieve very high specific energy.

However, the trends so far only consider the bare cells without current collectors. The additional weight introduced when current-collector foils are required affects the conversion-type cells more than the higher voltage intercalation-type cells. The influence is so strong that any Li–S ASSB that uses a copper and an aluminium current collector of 15- $\mu\text{m}$  thickness each per cell, must achieve lower cell resistance than a higher voltage intercalation-type cell for the same specific energy.

Due to the reasons stated above, we have so far focused on the specific energy of ASSBs. However, depending on the application, volume limitations may be critical, thus making the attainable energy density the decisive factor. Our equivalent analysis of the energy density versus the required internal resistance is shown in Supplementary Fig. 15. The results demonstrate that, here, conversion-type cell systems are at a striking disadvantage over higher voltage systems, underlining the emphasis that the automotive industry places on high-voltage cell systems.

Overall, this comparison demonstrates the importance of developing cells with thinner separators and better processing techniques to achieve the internal resistance and current density requirements for high energy and high power ASSBs. At 200- $\mu\text{m}$  separator thickness, achieving this appears improbable unless substantial advances in solid electrolyte ionic conductivity are made. Reducing excess cell weight, for example, by bipolar stacking, might prove especially important for conversion-type cells to achieve exceptionally high specific energy where cell weight plays a critical role, such as in aerospace applications.

### Research targets

From the above analysis, it seems that all the necessary tools are now at hand to obtain a pellet-type ASSB with more than  $250 \text{ Wh kg}^{-1}$  and stable cycling by combining  $\text{LiNbO}_3$ -protected  $\text{LiCoO}_2$  as the positive electrode<sup>26</sup>, a thiophosphate solid electrolyte<sup>13,15</sup> and protected lithium



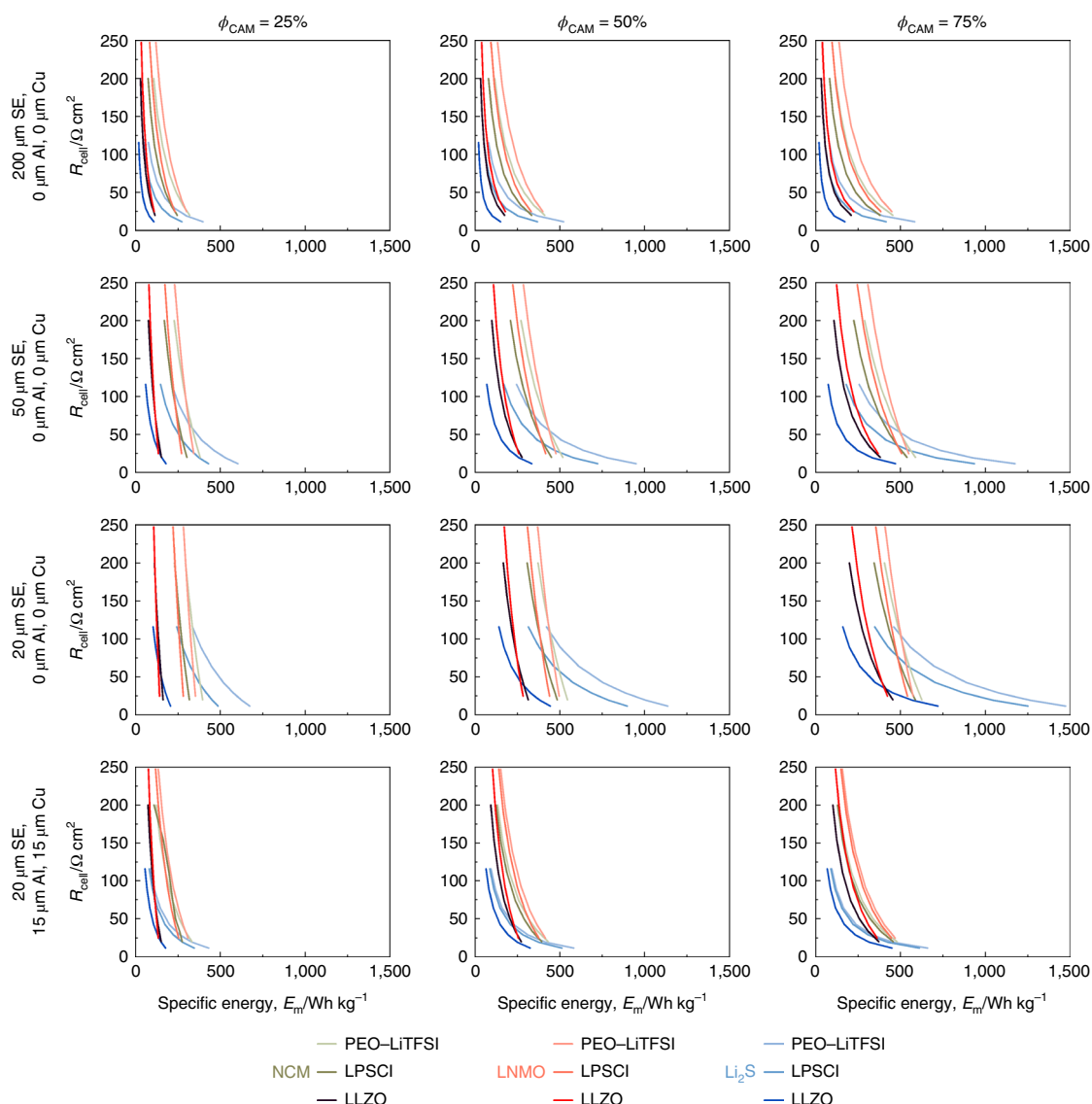


**Fig. 4 | The maximum allowed internal resistance and achievable specific energy for intercalation- and conversion-type cell systems.** These are calculated by varying the area capacity using Supplementary Data 3. NCM, LNMO and  $\text{Li}_2\text{S}$  cathode materials and solid electrolytes PEO-LiTFSI (density of  $1.2 \text{ g cm}^{-3}$ ),  $\text{Li}_6\text{PS}_5\text{Cl}$  (LPSCI, density of  $1.87 \text{ g cm}^{-3}$ ) and  $\text{Li}_7\text{La}_3\text{Zr}_2\text{O}_{12}$  (LLZO, density of  $5.14 \text{ g cm}^{-3}$ ) are compared. Theoretical specific capacity of each CAM is assumed. Each point (area capacity) indicates the achievable specific energy and the internal resistance requirement for 90% energy efficiency at a rate of 1C. A thickness of  $20 \mu\text{m}$  of lithium foil is used for this calculation. Comparison is carried out at equal current density, that is, equal area capacity. Hence, variation of the cathode composite thickness is required to set cell capacity to 1.0, 1.3, 1.8, 2.7, 4.0, 6.0 or  $10.0 \text{ mAh cm}^{-2}$  (low to high specific energy). Values of 200, 50 or  $20 \mu\text{m}$  solid electrolyte, 25 vol%, 50 vol% or 75 vol% volume fraction  $\phi_{\text{CAM}}$  of CAM in the cathode composite and the addition of aluminium and copper foil current collectors (each  $15 \mu\text{m}$  thick) are compared by modifying the input parameters in Supplementary Data 3.

metal as the negative electrode<sup>20</sup> (see example 4 in Supplementary Data 2). However, the specific energy is not the only parameter of importance. A high specific power beyond  $250 \text{ W kg}^{-1}$  requires cells with less than about  $40 \Omega \text{ cm}^2$  of internal resistance. Optimizing cell design will play an important role in achieving these targets.

Comparing the requirements obtained from performance prediction with our literature survey indicates what has already been achieved and which targets still need to be met. This identifies the research goals listed in Table 4. An important problem yet to be solved in the solid state is accessing the theoretical specific capacity of CAMs. For example, the theoretical specific capacity of NCM has been shown to be about  $200 \text{ mAh g}^{-1}$  in cells using liquid electrolytes<sup>50</sup>, while ASSBs with NCM struggle to exceed  $150 \text{ mAh g}^{-1}$  at ambient temperature. Furthermore, CAM content in the composite

cathode needs to be increased to maximize hypothetical specific energy<sup>51,52</sup>. The development of highly conducting ( $>10 \text{ mS cm}^{-1}$ ), electrochemically compatible solid electrolytes will help with these targets. Also, new coatings for NCM-type CAMs are to be developed to reduce charge transfer resistance and increase capacity retention. New processing methods will allow creation of larger cells. Important targets for conversion-type cells are increased cell voltage, reduced internal resistance, increased CAM content, decreased separator thickness and increased current density.

On the anode side, formation of a lithium metal anode in situ, without the initial addition of lithium foil, would substantially increase energy density and facilitate cell manufacturing<sup>53</sup>. Also, lithium dendrite growth is expected to occur at higher current densities. Therefore, it is important to develop reliable methods

**Table 4 | Research targets to achieve high energy and power ASSBs**

Parameter	Target description
Cell voltage, $V$	Lithium metal has been identified as the key anode material. Development of intercalation-type CAMs, such as NCM or LNMO, to achieve high energy density, and conversion-type CAMs, to achieve high specific energy, is ongoing.
Specific capacity, $q$	Practical specific capacity needs to reach theoretical values at ambient temperature, for example, NCM $\sim 200 \text{ mAh g}^{-1}$ , $\text{Li}_2\text{S}$ $1,166 \text{ mAh g}^{-1}$ , LNMO $147 \text{ mAh g}^{-1}$ .
Volume fraction of CAM in cathode composite, $\phi_{\text{CAM/Ca}}$	Most studies apply a volume fraction of CAM of 40–60 vol% in the cathode composite. Increasing this to more than 70 vol% is an important target to increase specific energy and energy density <sup>51,52</sup> .
Hypothetical specific energy, $E_{\text{m(Ca)}}$ , and area capacity, $Q_{\text{A}}$	These are the key to maximize specific energy and energy density. Cathode composites exceeding $500 \text{ Wh kg}^{-1}$ (versus $\text{Li}^+/\text{Li}$ by weight of cathode composite only) and $5 \text{ mAh m}^{-2}$ are desired.
Current density, $j$	Dendrite formation needs to be prevented at a current density of at least $5 \text{ mA cm}^{-2}$ (refs. <sup>49,54</sup> ).
Energy efficiency, $\Phi_{\text{E}}$	The desired energy efficiency determines the allowed overvoltage. Using Ohm's law, the maximum allowed internal resistance of the cell is estimated from the allowed overvoltage and the desired current density. More than 90% should be achieved.
Internal resistance, $R$	A high specific energy cell requires less than about $40 \Omega \text{ cm}^2$ internal resistance to allow cycling at 1C with more than 90% energy efficiency <sup>3</sup> .
Lithium thickness, $l_{\text{An}}$	Concepts of reducing lithium layer thickness are under development <sup>60</sup> . Ideally, introduction of excess lithium would not be required and lithium would stem solely from the CAM.
Solid electrolyte thickness, $l_{\text{SE}}$	Solid electrolyte thickness of as little as $30 \mu\text{m}$ has been demonstrated <sup>21,48</sup> . Further reducing layer thickness increases specific energy and reduces internal resistance.
Cathode composite thickness, $l_{\text{Ca}}$	The thickness of the composite cathode requires a balance of increasing specific energy of the cell by increasing thickness, while remaining within a practical window for the required current density.
Cell area, $A$	Thin composite cathodes and solid electrolyte separators can be prepared at small scale. Creation of the lithium metal anode in a pouch-type set-up with inorganic electrolytes remains a challenge. Large-area cells with more than $200 \text{ cm}^2$ remain to be demonstrated for ASSBs with inorganic electrolytes <sup>15,52</sup> .
Pressure, $p$	The most successful ASSBs so far applied external pressure during cycling of the cell. For practical applications, the requirement for excessive pressure should be avoided.
Additives	The roles of binders and conductive carbon additives need to be investigated further <sup>55–57</sup> .
Energy retention	Cycling tests aim to demonstrate a cell that maintains more than 80% of its original specific energy over 1,000 cycles and at least $5 \text{ Wh cm}^{-2}$ delivered area energy.

to prevent lithium dendrite formation up to at least  $10 \text{ mA cm}^{-2}$  (ref. <sup>54</sup>). Finally, a discussion of binders and conductive carbon additives was beyond the scope of our analysis, but their influence on cell performance and cell degradation must also be investigated further<sup>55–57</sup>. With these challenges solved, excluding cell casing, ASSBs with specific energy beyond  $400 \text{ Wh kg}^{-1}$ , energy density beyond  $1,000 \text{ Wh l}^{-1}$  and more than 90% energy efficiency at a 1C rate are within reach (Fig. 4 and Supplementary Fig. 15).

## Conclusions

Starting out with a survey of the ASSB literature, it is evident that a comparison of cell performance is not always directly accessible. Therefore, we present an extensive analysis of the performance measures of the best-performing all-solid-state batteries in our literature overview. This demonstrates that the differences in specific energy and specific power of the multitude of available ASSBs mostly originate from differences in layer thicknesses and internal resistance. To compare these with a basic reference system, we present an all-solid-state battery using only a lithium metal anode,  $\beta\text{-Li}_3\text{PS}_4$  solid electrolyte and  $\text{Li}(\text{Ni}_{0.6}\text{Co}_{0.2}\text{Mn}_{0.2})\text{O}_2$  cathode active material. We intentionally did not apply material coatings or carbon additives so that these cells can serve as minimalistic references. The Ragone plot and the plot of the cycle-dependent specific discharge energy offer direct comparison of different cell chemistries and varying cycling protocols relative to our minimalistic cells. This demonstrates that high specific energy and high specific power ASSBs using lithium metal remain elusive as long as thick separators are used. Cycling tests show that further research is required to develop protective

coatings, especially for high-voltage CAMs. Using the fundamental equations that determine battery performance, we identify and quantify key research targets, such as achieving less than  $40 \Omega \text{ cm}^2$  internal resistance, less than  $50 \mu\text{m}$  separator thickness, in-situ generation of the anode, more than  $5 \text{ mAh cm}^{-2}$  area capacity and  $500 \text{ Wh kg}^{-1}$  hypothetical cathode specific energy. Thus, our analysis projects a pathway to lithium metal ASSBs and highlights the remaining challenges still to be overcome in order to surpass the performance of state-of-the-art lithium-ion batteries.

## Methods

**Literature analysis.** We include all ASSBs from the literature that allowed us to carry out a consistent full cell analysis (Tables 1 and 2). In some cases, we selected representative examples, as the inclusion of all reports would have exceeded the scope of this analysis. Most of the cells included in our analysis are not optimized for energy and power, which we ask the reader to bear in mind when interpreting the results. To obtain all parameters for the literature overview, we identified the parameters available in each publication individually and calculated the remaining parameters one by one to complete the set. In some cases, we had to make assumptions to approximate unavailable parameters, as described in Supplementary Table 2.

**Calculating performance measures.** As summarized in Supplementary Data 1, the experimental data obtained for cell type 1 and 2 are used as input parameters (highlighted in grey) to calculate the corresponding performance measures (highlighted in colour) in the same line. The underlying formula can be identified by double-clicking on the respective cell. The calculation is set up such that the performance measures are automatically calculated from the input parameters of the same row. Exception: at least two consistent consecutive lines of data are required to correctly calculate efficiency, cumulative and retention parameters for cell cycling analysis. An explanation of the symbols and columns is given in the tab labelled 'legend' of the Supplementary Data 1.

Using Supplementary Data 1, the reader can easily analyse their own experiments by replacing the data for the input parameters with the corresponding complete set of their own data. The resulting performance indicators are then automatically calculated using the embedded formula and cell references. To add additional rows with full functionality for analysis, simply copy complete rows of data into rows without data or select the filled cells to be used for the calculation and drag the fill handle upwards or downwards.

To gauge the performance potential of solid-state batteries by calculating examples 1 to 4 described in the section on 'Performance prediction', we demonstrate thought experiments for all-solid-state lithium batteries in Supplementary Data 2. Supplementary Data 2 functions, in principle, in the same way as Supplementary Data 1. However, instead of experimental data used as the input parameters, values are varied within reason to predict the corresponding performance measures.

In Supplementary Data 3, we calculate the achievable specific energy for intercalation- and conversion-type lithium ASSBs and the corresponding maximum allowed internal resistance and the minimum required current density. The results are used to calculate the data for Fig. 4 and Supplementary Figs. 14 and 15 by varying the input parameters within reason (see Supplementary Table 9). Supplementary Data 3 functions, in principle, in the same way as Supplementary Data 1. The reader can modify the input parameters, to match their interest. The figures included in the spreadsheet table are updated automatically, as are the corresponding performance measures.

All three spreadsheets can, in principle, also be applied to other battery types and can be modified to accommodate additional performance measures of interest.

**Materials.** BASF SE provided the crystalline solid electrolyte  $\beta$ -Li<sub>3</sub>PS<sub>4</sub> ( $1.2 \times 10^{-4} \text{ S cm}^{-1}$ ) and the Li(Ni<sub>0.6</sub>Co<sub>0.3</sub>Mn<sub>0.2</sub>)O<sub>2</sub> (NCM) active material for this study. All chemicals were stored in an argon-filled glovebox (H<sub>2</sub>O < 0.1 ppm and O<sub>2</sub> < 0.1 ppm). X-ray diffraction patterns and scanning electron microscopy (SEM) images of LPS and NCM are available in Supplementary Figs. 16–19. The NCM active material was dried in a vacuum at 250 °C (Büchi furnace) overnight. A disc of lithium foil of approximately 120  $\mu\text{m}$  thickness and 9 mm diameter was used as the anode. The composite cathode consists of dried NCM ( $\rho = 4.78 \text{ g cm}^{-3}$ )<sup>58</sup> and  $\beta$ -Li<sub>3</sub>PS<sub>4</sub> ( $\rho = 1.83 \text{ g cm}^{-3}$ )<sup>59</sup> in a mass ratio of 70:30 (volume ratio 47:53). The NCM and LPS powders were ground in an agate mortar for 15 min by hand before cell assembly, forming the cathode mixture.

**Li | LPS | NCM cell assembly.** The cell casing was manufactured in-house as described in detail previously<sup>42,43</sup>. The Li |  $\beta$ -Li<sub>3</sub>PS<sub>4</sub> | NCM:  $\beta$ -Li<sub>3</sub>PS<sub>4</sub> (Li | LPS | NCM:LPS) cells (Supplementary Fig. 1) were assembled within an argon-filled glovebox. For cell assembly, one of the stainless steel stamp current collectors was used to close one side of a polyether ether ketone cylinder with a diameter of 10 mm, into which all materials were added via the remaining opening. First, 60 mg of the  $\beta$ -Li<sub>3</sub>PS<sub>4</sub> solid electrolyte was added and the powder was uniformly compressed manually with the second stainless steel stamp current collector. Then, 10 mg of cathode composite (NCM:LPS was 70:30 by weight;  $8.9 \text{ mg cm}^{-2}$ ) was distributed evenly on top of the smooth LPS surface, corresponding to an area capacity of  $1.78 \text{ mAh cm}^{-2}$  on the basis of a theoretical specific capacity of  $200 \text{ mAh g}_{\text{CAM}}^{-1}$  (ref. <sup>60</sup>). For cells with higher area capacity, the amounts of LPS and cathode composite were modified as specified in the respective section. The stack was then compressed uniaxially between the stainless steel stamp current collectors at 30 kN (that is,  $\sim 380 \text{ MPa}$ , for cells with higher area capacity the pressure needed to be reduced to 25 kN) for 3 min before adding the lithium disc anode (thickness: 120  $\mu\text{m}$ , diameter: 9 mm) and a copper foil disc (thickness: 40  $\mu\text{m}$ , diameter: 10 mm) to the cell illustrated in Supplementary Fig. 1. The copper foil is used for stabilization of the battery stack during disassembly. Without copper foil, lithium would stick to the steel current collectors and complete removal of the battery would be impossible, complicating post-experiment analysis. Finally, a pressure of approximately 50 MPa was applied using an external frame, which remained in place during all electrochemical measurements.

**Electrochemical characterization.** Charge and discharge tests were performed using a VMP-300 Biologic and a MACCOR potentiostat/galvanostat. Cells using lithium as anode material were repeatedly charged galvanostatically to 4.3 V and discharged to 2.6 V versus Li<sup>+/</sup>Li at 25 °C. The applied current density was  $0.178 \text{ mA cm}^{-2}$  corresponding to a 0.1C rate for cells with an area capacity of  $1.78 \text{ mAh cm}^{-2}$ . For the rate test and cells with higher area capacity, the current density was modified accordingly. Electrochemical impedance spectroscopy (EIS) was performed using an EC-Lab Electrochemistry VMP-300 Biologic before the first charge step and for the first five cycles after reaching the cut-off voltages and 10 min of pause (open circuit voltage measurement). EIS was conducted in the frequency range 7 MHz to 1 Hz, applying a 10-mV signal amplitude.

**X-ray photoelectron spectroscopy.** X-ray photoelectron spectroscopy (XPS) was employed to identify decomposition products and the binding states of the used battery materials. The measurements were carried out using a PHI5000 Versa Probe II with an Al anode. Exposure to air was avoided by using a transfer vessel filled with argon, which was loaded inside the argon-filled glovebox. A surface area of  $100 \mu\text{m} \times 1,400 \mu\text{m}$  (X-ray spot size) was investigated and an X-ray power of 100 W

was used. The pass energy of the analyser was set to 187.9 eV for survey scans and 23.5 eV for detailed spectra. A charge correction was carried out for all spectra, to a binding energy of 284.8 eV referring to the C 1s line corresponding to adventitious carbon. CasaXPS v.2.3.17 software was used to evaluate the received spectra.

**SEM of battery cross-sections.** The all-solid-state battery was cut in half using an ultrasonic knife (Sonofile, SF-0102) and the received cross-section was analysed by SEM. The SEM images of the cross-sections did not show signs of mixing of the different battery materials due to the cutting process, that is, clean cross-sections were obtained, the cutting area was sharp and there was no smearing of materials. Microstructure images of disassembled battery components were obtained on a high-resolution scanning electron microscope (Merlin, Carl Zeiss AG). An acceleration voltage of 3 kV and a sample current of 150 pA were applied. The secondary electron detector was used to record the images.

**Distribution of relaxation times (DRT) analysis.** Previous publications<sup>61,62</sup> have shown that it is favourable to deconvolute impedance data in the space of relaxation times. This so-called DRT method enables a refined separation of physical processes even if they are strongly overlapping in the Nyquist diagram. Each process is represented as a local maximum in a continuous distribution function. The advantage is that processes with close time constants can be separated and a physically motivated equivalent circuit model can be established. Furthermore, Schönleber et al.<sup>63</sup> proved that any non-oscillating electrochemical system can be correctly described using the DRT.

## Data availability

All data generated or analysed during this study are included in this Analysis and its Supplementary Information files.

Received: 14 May 2019; Accepted: 24 January 2020;

Published online: 09 March 2020

## References

- Schmich, R., Wagner, R., Hörpel, G., Placke, T. & Winter, M. Performance and cost of materials for lithium-based rechargeable automotive batteries. *Nat. Energy* **3**, 267–278 (2018).
- Hayashi, A., Noi, K., Sakuda, A. & Tatsumisago, M. Superionic glass-ceramic electrolytes for room-temperature rechargeable sodium batteries. *Nat. Commun.* **3**, 856 (2012).
- Kato, Y. et al. High-power all-solid-state batteries using sulfide superionic conductors. *Nat. Energy* **1**, 16030 (2016).
- Yu, S. et al. Monolithic all-phosphate solid-state lithium-ion battery with improved interfacial compatibility. *ACS Appl. Mater. Interfaces* **10**, 22264–22277 (2018).
- Finsterbusch, M. et al. High capacity garnet-based all-solid-state lithium batteries: fabrication and 3D-microstructure resolved modeling. *ACS Appl. Mater. Interfaces* **10**, 22329–22339 (2018).
- Yao, X. et al. High-energy all-solid-state lithium batteries with ultralong cycle life. *Nano Lett.* **16**, 7148–7154 (2016).
- Hovington, P. et al. New lithium metal polymer solid state battery for an ultrahigh energy: nano C-LiFePO<sub>4</sub> versus nano Li<sub>1.2</sub>V<sub>3</sub>O<sub>8</sub>. *Nano Lett.* **15**, 2671–2678 (2015).
- Krauskopf, T., Hartmann, H., Zeier, W. G. & Janek, J. Toward a fundamental understanding of the lithium metal anode in solid-state batteries—an electrochemo-mechanical study on the garnet-type solid electrolyte Li<sub>6.25</sub>Al<sub>0.25</sub>La<sub>2</sub>Zr<sub>2</sub>O<sub>12</sub>. *ACS Appl. Mater. Interfaces* **11**, 14463–14477 (2019).
- Zhu, G.-L. et al. Fast charging lithium batteries: recent progress and future prospects. *Small* **15**, 1805389 (2019).
- Liu, J. et al. Pathways for practical high-energy long-cycling lithium metal batteries. *Nat. Energy* **4**, 180–186 (2019).
- Takeda, Y., Yamamoto, O. & Imanishi, N. Lithium dendrite formation on a lithium metal anode from liquid, polymer and solid electrolytes. *Electrochemistry* **84**, 210–218 (2016).
- Porz, L. et al. Mechanism of lithium metal penetration through inorganic solid electrolytes. *Adv. Energy Mater.* **7**, 1–12 (2017).
- Zhu, Y., He, X. & Mo, Y. Strategies based on nitride materials chemistry to stabilize Li metal anode. *Adv. Sci.* **4**, 1–11 (2017).
- Culver, S. P., Koerver, R., Zeier, W. G. & Janek, J. On the functionality of coatings for cathode active materials in thiophosphate-based all-solid-state batteries. *Adv. Energy Mater.* **9**, 1900626 (2019).
- Nam, Y. J., Oh, D. Y., Jung, S. H. & Jung, Y. S. Toward practical all-solid-state lithium-ion batteries with high energy density and safety: comparative study for electrodes fabricated by dry- and slurry-mixing processes. *J. Power Sources* **375**, 93–101 (2018).
- Sakuda, A. et al. All-solid-state battery electrode sheets prepared by a slurry coating process. *J. Electrochem. Soc.* **164**, A2474–A2478 (2017).
- Ma, J., Chen, B., Wang, L. & Cui, G. Progress and prospect on failure mechanisms of solid-state lithium batteries. *J. Power Sources* **392**, 94–115 (2018).

18. Kerman, K., Luntz, A., Viswanathan, V., Chiang, Y.-M. & Chen, Z. Review—practical challenges hindering the development of solid state Li ion batteries. *J. Electrochem. Soc.* **164**, A1731–A1744 (2017).
19. Whiteley, J., Woo, J. H., Hu, E., Nam, K. & Lee, S. Empowering the lithium metal battery through a silicon-based superionic conductor. *J. Electrochem. Soc.* **161**, A1812–A1817 (2014).
20. Zhang, Z. et al. Interface re-engineering of  $\text{Li}_{10}\text{GeP}_2\text{S}_{12}$  electrolyte and lithium anode for all-solid-state lithium batteries with ultralong cycle life. *ACS Appl. Mater. Interfaces* **10**, 2556–2565 (2018).
21. Woo, J. et al. Nanoscale interface modification of  $\text{LiCoO}_2$  by  $\text{Al}_2\text{O}_3$  atomic layer deposition for solid-state Li batteries. *J. Electrochem. Soc.* **159**, A1120–A1124 (2012).
22. Xie, D. et al. High ion conductive  $\text{Sb}_2\text{O}_3$ -doped  $\beta\text{-Li}_3\text{PS}_4$  with excellent stability against Li for all-solid-state lithium batteries. *J. Power Sources* **389**, 140–147 (2018).
23. Ulissi, U., Agostini, M., Ito, S., Aihara, Y. & Hassoun, J. All solid-state battery using layered oxide cathode, lithium-carbon composite anode and thio-LISICON electrolyte. *Solid State Ionics* **296**, 13–17 (2016).
24. Choi, S.-J. et al. LiI-doped sulfide solid electrolyte: enabling a high-capacity slurry-cast electrode by low-temperature post-sintering for practical all-solid-state lithium batteries. *ACS Appl. Mater. Interfaces* **10**, 31404–31412 (2018).
25. Yamamoto, M., Terauchi, Y., Sakuda, A. & Takahashi, M. Binder-free sheet-type all-solid-state batteries with enhanced rate capabilities and high energy densities. *Sci. Rep.* **8**, 1212 (2018).
26. Kato, Y. et al. All-solid-state batteries with thick electrode configurations. *J. Phys. Chem. Lett.* **9**, 607–613 (2018).
27. Ito, S. et al. A rocking chair type all-solid-state lithium ion battery adopting  $\text{Li}_2\text{O-ZrO}_2$  coated  $\text{LiNi}_{0.8}\text{Co}_{0.15}\text{Al}_{0.05}\text{O}_2$  and a sulfide based electrolyte. *J. Power Sources* **248**, 943–950 (2014).
28. Kim, D. et al. Infiltration of solution-processable solid electrolytes into conventional Li-ion-battery electrodes for all-solid-state Li-ion batteries. *Nano Lett.* **17**, 3013–3020 (2017).
29. Kraft, M. A. et al. Inducing high ionic conductivity in the lithium superionic argyrodites  $\text{Li}_{6+x}\text{P}_{1-x}\text{Ge}_2\text{S}_6\text{I}$  for all-solid-state batteries. *J. Am. Chem. Soc.* **140**, 16330–16339 (2018).
30. Yamada, T. et al. All solid-state lithium–sulfur battery using a glass-type  $\text{P}_2\text{S}_5\text{-Li}_2\text{S}$  electrolyte: benefits on anode kinetics. *J. Electrochem. Soc.* **162**, A646–A651 (2015).
31. Zhang, Q. et al. Nickel sulfide anchored carbon nanotubes for all-solid-state lithium batteries with enhanced rate. *J. Mater. Chem. A* **6**, 12098–12105 (2018).
32. Chen, R. et al. Addressing the interface issues in all-solid-state bulk-type lithium ion battery via an all-composite approach. *ACS Appl. Mater. Interfaces* **9**, 9654–9661 (2017).
33. Park, M., Jung, Y. & Kim, D. Hybrid solid electrolytes composed of poly(1,4-butylene adipate) and lithium aluminum germanium phosphate for all-solid-state  $\text{Li/LiNi}_{0.6}\text{Co}_{0.2}\text{Mn}_{0.2}\text{O}_2$  cells. *Solid State Ionics* **315**, 65–70 (2018).
34. Wakayama, H., Yonekura, H. & Kawai, Y. Three-dimensional bicontinuous nanocomposite from a self-assembled block copolymer for a high-capacity all-solid-state lithium battery cathode. *Chem. Mater.* **28**, 4453–4459 (2016).
35. Ates, T., Keller, M., Kulisch, J., Adermann, T. & Passerini, S. Development of an all-solid-state lithium battery by slurry-coating procedures using a sulfidic electrolyte. *Energy Storage Mater.* **18**, 31261–31264 (2018).
36. Porcarelli, L. et al. Single-ion triblock copolymer electrolytes based on poly(ethylene oxide) and methacrylic sulfonamide blocks for lithium metal batteries. *J. Power Sources* **364**, 191–199 (2017).
37. Bouchet, R. et al. Single-ion BAB triblock copolymers as highly efficient electrolytes for lithium-metal batteries. *Nat. Mater.* **12**, 452–457 (2013).
38. Kim, J., Hong, Y., Ryu, K. S., Kim, M. G. & Cho, J. Washing effect of a  $\text{LiNi}_{0.83}\text{Co}_{0.15}\text{Al}_{0.02}\text{O}_2$  cathode in water. *Electrochem. Solid-State Lett.* **9**, A19–A23 (2006).
39. Visbal, H. et al. The influence of the carbonate species on  $\text{LiNi}_{0.8}\text{Co}_{0.15}\text{Al}_{0.05}\text{O}_2$  surfaces for all-solid-state lithium ion battery performance. *J. Power Sources* **269**, 396–402 (2014).
40. Liu, Z. et al. Anomalous high ionic conductivity of nanoporous  $\beta\text{-Li}_3\text{PS}_4$ . *J. Am. Chem. Soc.* **135**, 975–978 (2013).
41. Phuc, N. H. H., Morikawa, K., Mitsuhiro, T., Muto, H. & Matsuda, A. Synthesis of plate-like  $\text{Li}_3\text{PS}_4$  solid electrolyte via liquid-phase shaking for all-solid-state lithium batteries. *Solid State Ionics* **23**, 2061–2067 (2017).
42. Zhang, W. et al. Interfacial processes and influence of composite cathode microstructure controlling the performance of all-solid-state lithium batteries. *ACS Appl. Mater. Interfaces* **9**, 17835–17845 (2017).
43. Koerver, R. et al. Capacity fade in solid-state batteries: interphase formation and chemomechanical processes in nickel-rich layered oxide cathodes and lithium thiophosphate solid electrolytes. *Chem. Mater.* **29**, 5574–5582 (2017).
44. Ragone, D. V. *Review of Battery Systems for Electrically Powered Vehicles* SAE Technical Paper 680453 (SAE, 1968).
45. van Noorden, R. A better battery. *Nature* **507**, 26–28 (2014).
46. Sanyo Energy. *Panasonic NCR18650B Specification* (2012); <https://www.batteryspace.com/prod-specs/NCR18650B.pdf>.
47. Keller, M., Varzi, A. & Passerini, S. Hybrid electrolytes for lithium metal batteries. *J. Power Sources* **392**, 206–225 (2018).
48. Fu, K. (K). Three-dimensional bilayer garnet solid electrolyte based high energy density lithium metal-sulfur batteries. *Energy Environ. Sci.* **10**, 1568–1575 (2017).
49. Fan, X. et al. Fluorinated solid electrolyte interphase enables highly reversible solid-state Li metal battery. *Sci. Adv.* **4**, eaau9245 (2018).
50. Chen, S. et al. High-efficiency lithium metal batteries with fire-retardant electrolytes. *Joule* **2**, 1–11 (2018).
51. Sakuda, A., Hayashi, A., Ohtomo, T., Hama, S. & Tatsumisago, M. All-solid-state lithium secondary batteries using  $\text{LiCoO}_2$  particles with pulsed laser deposition coatings of  $\text{Li}_2\text{S-P}_2\text{S}_5$  solid electrolytes. *J. Power Sources* **196**, 6735–6741 (2011).
52. Hippauf, F. et al. Overcoming binder limitations of sheet-type solid-state cathodes using a solvent-free dry-film approach. *Energy Storage Mater.* **21**, 390–398 (2019).
53. Krauskopf, T. et al. Lithium-metal growth kinetics on LLZO garnet-type solid electrolytes. *Joule* **3**, 2030–2049 (2019).
54. Albertus, P., Babinec, S., Litzelman, S. & Newman, A. Status and challenges in enabling the lithium metal electrode for high-energy and low-cost rechargeable batteries. *Nat. Energy* **3**, 16–21 (2018).
55. Yoon, K., Kim, J.-J., Seong, W. M., Lee, M. H. & Kang, K. Investigation on the interface between  $\text{Li}_{10}\text{GeP}_2\text{S}_{12}$  electrolyte and carbon conductive agents in all-solid-state lithium battery. *Sci. Rep.* **8**, 8066 (2018).
56. Zhang, W. et al. The detrimental effects of carbon additives in  $\text{Li}_{10}\text{GeP}_2\text{S}_{12}$ -based solid-state batteries. *ACS Appl. Mater. Interfaces* **9**, 35888–35896 (2017).
57. Hakari, T., Sato, Y., Yoshimi, S., Hayashi, A. & Tatsumisago, M. Favorable carbon conductive additives in  $\text{Li}_3\text{PS}_4$  composite positive electrode prepared by ball-milling for all-solid-state lithium batteries. *J. Electrochem. Soc.* **164**, A2804–A2811 (2017).
58. Huang, Z. et al. Structural and electrochemical properties of Mg-doped nickel based cathode materials  $\text{LiNi}_{0.6}\text{Co}_{0.2}\text{Mn}_{0.2-x}\text{Mg}_x\text{O}_2$  for lithium ion batteries. *RSC Adv.* **5**, 88773–88779 (2015).
59. Homma, K. et al. Crystal structure and phase transitions of the lithium ionic conductor  $\text{Li}_3\text{PS}_4$ . *Solid State Ionics* **182**, 53–58 (2011).
60. Nitta, N., Wu, F., Lee, J. T. & Yushin, G. Li-ion battery materials: present and future. *Mater. Today* **18**, 252–264 (2015).
61. Schichlein, H., Müller, A. C., Voigts, M., Krügel, A. & Ivers-Tiffée, E. Deconvolution of electrochemical impedance spectra for the identification of electrode reaction mechanisms in solid oxide fuel cells. *J. Appl. Electrochem.* **32**, 875–882 (2002).
62. Ivers-Tiffée, E. & Weber, A. Evaluation of electrochemical impedance spectra by the distribution of relaxation times. *J. Ceram. Soc. Jpn* **125**, 193–201 (2017).
63. Schönleber, M. & Ivers-Tiffée, E. Approximability of impedance spectra by RC elements and implications for impedance analysis. *Electrochem. Commun.* **58**, 15–19 (2015).

## Acknowledgements

Financial support from the Federal Ministry of Education and Research (BMBF) within the FELIZIA project (grant nos. 03XP0026G and 03XP0026J) and the FESTBATT consortium (grant no. 03XP0177A) is acknowledged. We acknowledge discussions with T. Ates, S. Culver, C. Dietrich, M. Keller, P. Minnmann, C. Pompe, N. Rippaus, J. Sann and M. Weiß.

## Author contributions

S.R., D.A.W., W.G.Z., F.H.R. and J.J. designed the experimental work. S.R. and O.K. conducted the experimental work. R.K. carried out and analysed the XPS measurements. P.B., A.W. and E.I.-T. carried out the DRT analysis. T.A. and J.K. provided the solid electrolyte and cathode active material. S.R. and F.H.R. analysed the literature data and cell performance prediction. S.R., F.H.R. and J.J. wrote the manuscript. F.H.R. and J.J. directed this work. All authors commented on the manuscript.

## Competing interests

D.A.W. is now employed by Volkswagen AG and R.K. is now employed by BMW group.

## Additional information

**Supplementary information** is available for this paper at <https://doi.org/10.1038/s41560-020-0565-1>.

**Correspondence and requests for materials** should be addressed to F.H.R. or J.J.

**Reprints and permissions information** is available at [www.nature.com/reprints](http://www.nature.com/reprints).

**Publisher's note** Springer Nature remains neutral with regard to jurisdictional claims in published maps and institutional affiliations.

© The Author(s), under exclusive licence to Springer Nature Limited 2020